Supplementary Information

Binding of the Substrate Analog Methanol in the Oxygen-evolving Complex of Photosystem II in the D1-N87A Genetic Variant of Cyanobacteria

Vidmantas Kalendra,[a] Krystle M. Reiss,[b] Gourab Banerjee,[b] Ipsita Ghosh,[b] Amgalanbaatar Baldansuren,[a] Victor S. Batista,[b] Gary W. Brudvig[b,*] and K. V. Lakshmi[a,*]

[a]Department of Chemistry and Chemical Biology and The Baruch '60 Center for Biochemical Solar Energy Research, Rensselaer Polytechnic Institute, Troy, New York 12180, USA

[b]Department of Chemistry, Yale University, New Haven, Connecticut 06520, USA

1. Preparation of photosystem II complexes. As previously described, the D1-N87A variant was constructed in the psbA-2 gene of *Synechocystis* sp. PCC 6803 and transformed into a host strain of *Synechocystis* that lacks all three psbA genes and contains a $(His)_6$-tag at the C-terminus of the CP47 polypeptide.[1] The D1-N87A cells were grown on solid BG-11 medium containing 5 g/ml kanamycin monosulfate and 20 g/ml gentamycin sulfate in the absence of glucose. The liquid cultures[2] and the extraction and purification of PSII were performed as previously described.[3] The purified PSII core complexes (Chl concentration of ~ 1.2 mg/ml) were stored in a buffer solution containing 1.2 M betaine, 10% (v/v) glycerol, 50 mM MES-NaOH (pH 6.0), 20 mM $CaCl_2$, 5 mM $MgCl_2$, 50 mM histidine, 1 mM EDTA, and 0.03% (w/v) n-dodecyl-β-maltoside at -80 °C. Polymerase chain reaction amplification and sequencing of genomic DNA in the region of the psbA gene that contains the D1-N87 codon were performed on aliquots of each cell culture that was harvested to verify the integrity of the mutant cultures.[1] No trace of the wild-type codon was detected in any of the mutant cultures. Natural abundance ^{13}C or ^{13}C-labeled methanol was added to the final resuspension buffer of the cyanobacterial PSII to 5% (v/v).[4] The methanol treated samples were loaded into 4 mm O.D. quartz EPR tubes for pulsed EPR measurements. The methanol bound S_2 state of each sample was generated by illumination at 200 K for 8 minutes followed by rapid freezing at 77 K in the dark.

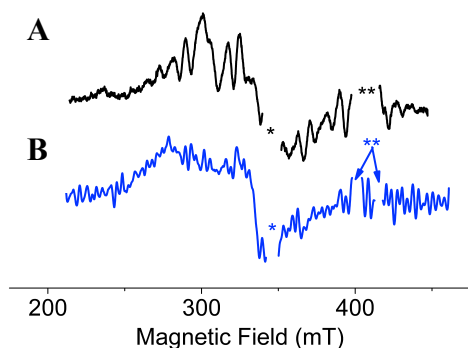**2. Light-induced EPR signals of WT and D1-N87A PSII**.

Figure 1S(A-B): Pseudo-modulated field-sweep electron-spin-echo EPR spectrum of the S_2 state of (A) untreated WT PSII and (B) ^{13}C-methanol bound D1-N87A PSII from *Synechocystis* sp. PCC 6803. In both cases, the S_2 multiline signal is centered at 340 mT (g = 2) with an overall spectral width of 200 mT. The signal-to-noise ratio of the S_2 multiline spectrum in part A is better due to a much higher sample concentration of

untreated WT PSII. The field positions marked by asterisks are background signals from the dark stable tyrosine-D radical of PSII and artifacts of the pulsed EPR resonator.

3. 2D ^{14}N and ^{13}C HYSCORE spectroscopy. The two-dimensional (2D) HYSCORE experiments were carried out at 5 K using a custom-designed X-band Bruker ELEXSYS E580 spectrometer equipped with an Oxford CF 935 helium flow cryostat. The 2D ^{14}N and ^{13}C HYSCORE spectra were acquired using a four-pulse ($\pi/2 - \tau - \pi/2 - t_1 - \pi - t_2 - \pi/2 - \tau - echo$) and six-pulse (($\pi/2)_y - \tau_1 - (\pi)_y - \tau_1 - (\pi/2)_x - t_1 - (\pi)_x - t_2 - (\pi/2)_x - \tau_2 - (\pi)_x - \tau_2 - (echo)_x$) sequence,[5] respectively, containing 256 × 256 points.[6-9] These sequences included appropriate phase cycling schemes to eliminate unwanted features from experimental echo envelopes. The latter sequence[10] has an advantage over the former since it can avoid the influence of the cross-suppression effect[11-13] on the weak modulation of I = 1/2 nuclei (e.g. ^{13}C) from the deep modulations of the ^{14}N nuclei. The length of the $\pi/2$- and π-pulse was 8 ns and 16 ns, respectively. The delays in the pulse sequence were defined as the difference in the starting point of the pulses. The echo intensity was measured as a function of t_1 and t_2, where t_1 and t_2 were incremented in steps of 16 ns from an initial value of 40 ns and 32 ns, respectively. The 8 ns time difference between the initial value of t_1 and t_2 was set to account for the difference in length between the $\pi/2$- and π-pulse. This provided symmetric spectra in both dimensions. The inter-pulse delays τ, τ_1 and τ_2 were 140 ns, 24 ns and 140 ns, respectively. Spectral processing of HYSCORE data, including baseline correction of relaxation decay by polynomial correction and apodization using a Hamming window was performed in Matlab R2019b. The 2D data was zero-filled to a 2048 × 2048 matrix prior to performing fast Fourier transformation. The appearance of off-diagonal cross-peaks in the ^{13}C HYSCORE spectra is described below.

The 2D HYSCORE technique measures nuclear transitions of hyperfine coupled NMR-active nuclei interacting with an $S = ^1/_2$ electron spin. There are two transitions with frequencies v_α and v_β for ^{13}C with nuclear spin of $I = ^1/_2$, corresponding to the two $m_s = \pm^1/_2$ manifolds of the electron spin of the manganese cluster in the S_2 state in the presence of an applied magnetic field. The value of these hyperfine frequencies depends on the vector sum of the applied magnetic field and local magnetic field induced on the ^{13}C nucleus by the isotropic and anisotropic hyperfine interactions with electron spin. These may produce a pair of cross-features (v_α, v_β) and (v_β, v_α) in the (+,+) quadrant, as well as a pair of features ($-v_\alpha$, v_β) and (v_α, $-v_\beta$) in the (−,+) quadrant of the

2D HYSCORE spectrum. The actual appearance of cross-peaks in the (+,+) or (−,+) quadrants is governed by the relative value of the ^{13}C hyperfine couplings and the nuclear Zeeman frequency, $^{13C}\nu$.[14, 15] The cross-peaks in the (−,+) quadrant arise primarily from strong hyperfine interactions, where, $|^{13C}A| > 2(^{13C}\nu)$, whereas peaks in the (+,+) quadrant are predominantly from interactions for which $|^{13C}A| < 2(^{13C}\nu)$. The cross-peaks may appear in both quadrants simultaneously for intermediate cases when the hyperfine interaction is comparable to the ^{13}C Zeeman frequency.[14]

The 2D ^{14}N and ^{13}C HYSCORE spectra were acquired at a magnetic field position of 335.0 mT. Due to the inhomogeneous broadening of the S_2 multiline peaks in Figure 1S, the spectral width clearly exceeds the excitation bandwidth of microwave pulses employed in the 2D HYSCORE experiments. In this case, the pulses lead to incomplete excitation of the EPR spectra, and thus orientationally-disordered cross-peaks or ridges are obtained that represent all possible orientations of the principal axes of ^{13}C hyperfine tensor(s) relative to the applied magnetic field. However, cross-peaks or ridges indicate the interdependence or correlation of ν_α and ν_β in the same orientation at the given magnetic field. The coordinates of any arbitrary point in the cross-peak or ridge are described in the first order by the equation:

$$\nu_{\alpha(\beta)} = |^{13C}\nu| \pm |^{13C}A|/2|$$

This can be used to estimate of the corresponding hyperfine coupling constant A as:

$$\nu_\alpha - \nu_\beta = |A| \text{ if } |^{13C}A| < 2(^{13C}\nu)$$

$$\nu_\alpha + \nu_\beta = |A| \text{ if } |^{13C}A| > 2(^{13C}\nu)$$

4. Spectral simulations. The experimental hyperfine values extracted from the raw experimental 2D HYSCORE spectra were used to simulate the positions and line widths of the off-diagonal cross-peaks C^I in the EasySpin v5.2.25[16, 17] package using Matlab R2019b. The excitation bandwidth of the microwave pulses was optimized during the simulation process. The strain-induced effects of the ^{13}C hyperfine interactions was modeled by previously described methods employing a triangle distribution function for the isotropic hyperfine coupling of hyperfine interaction tensors for a half-integer spin nucleus (^{13}C or ^{15}N).[18]

Table 1S: Complete set of simulation parameters for the 2D ^{13}C HYSCORE spectrum of the ^{13}C-methanol-bound S_2 state of D1-N87A PSII. The hyperfine coupling constants are in units of MHz.

Nucleus	A_{iso}	T	A_x	A_y	A_z	α	β	γ
^{13}C	3.63 ± 0.15	1.65 ± 0.11	2.4 ± 0.14	1.5 ± 0.12	7.0 ± 0.16	-22.8	59.6	1.7

5. 2D ^{14}N HYSCORE spectroscopy of the S_2 state of ^{13}C-methanol treated D1-N87A PSII from *Synechocystis* sp. PCC 6803.
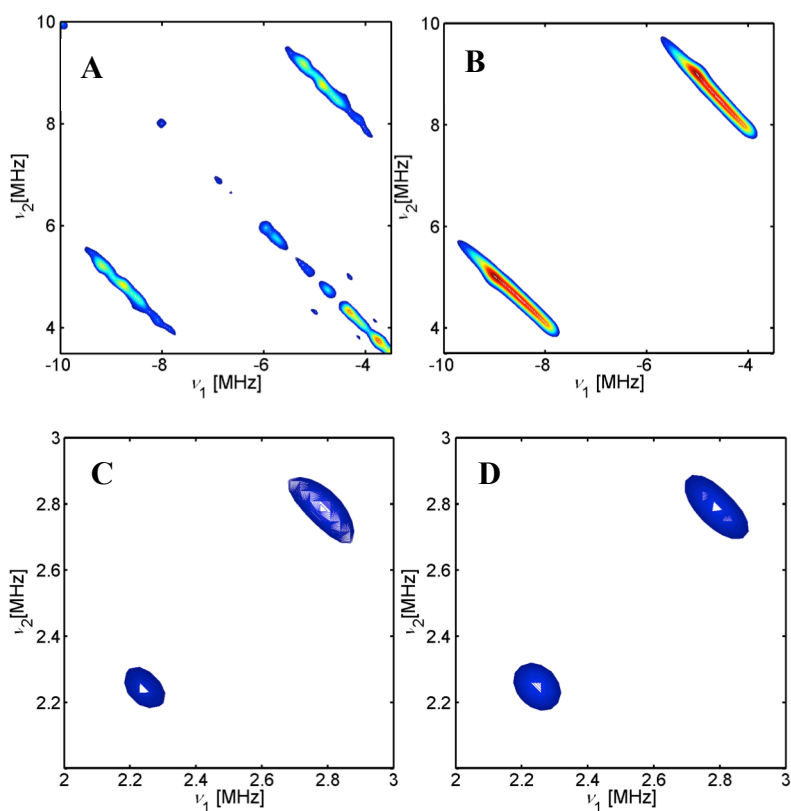

Figure 2S(A-D). Experimental and simulated contour-plot representation of the (A-B) (-,+) and (C-D) (+,+) quadrant of the 2D ^{14}N HYSCORE spectrum of the ^{13}C-methanol bound S_2 state of the OEC of D1-N87A PSII from *Synechocystis* sp. PCC 6803. The spectrum was acquired at a magnetic field of 335.0 mT and temperature of 5 K. The pair of cross-peaks in the (-,+) quadrant in parts A and B arise from the strongly hyperfine coupled imino nitrogen of the D1-H332 residue that is a ligand to the Mn1(III) ion. The

cross peaks in the (+,+) quadrant arise from weaker hyperfine couplings with a peptide nitrogen and the guanidyl nitrogen atoms of CP43-R357.[1, 7]

Table 2S. ^{14}N hyperfine and quadrupolar parameters of the S_2 state of methanol bound D1-N87A PSII. The hyperfine coupling constants are in units of MHz.

Nitrogen atom	A_x	A_y	A_z	A_{iso}	K	η
N^I	5.64	7.05	8.2	6.96 ± 0.21	0.50 ± 0.04	0.60 ± 0.05
N^{II}	0.18	0.1	0.01	0.10 ± 0.02	0.51 ± 0.03	0.76 ± 0.10
N^{III}	0.09	0.05	0.05	0.06 ± 0.04	0.24 ± 0.03	0.90 ± 0.07

6. 2D ^{13}C HYSCORE spectroscopy of the S_2 state of D1-N87A PSII from *Synechocystis* sp. PCC 6803.
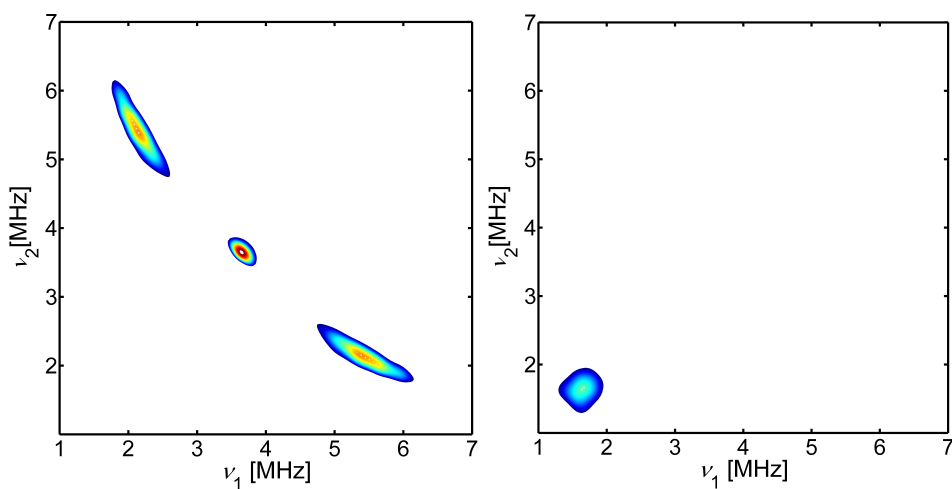

Figure 3S. Experimental contour-plot representation of the (+, +) quadrant of the 2D ^{13}C HYSCORE spectrum of the S_2 state of the OEC of (A) ^{13}C-methanol-treated and (B) untreated D1-N87A PSII from *Synechocystis* sp. PCC 6803. The spectrum was acquired at a magnetic field of 335.0 mT and temperature of 5 K. The intense cross-peaks at (5.4, 2.1) and (2.1, 5.4) MHz in part A are due to the hyperfine interactions of bound ^{13}C-methanol with the unpaired electron spin in the S_2 state of D1-N87A PSII. These are not observed in the untreated sample. Part A displays an S_2-minus-S_1 difference HYSCORE spectrum, while part B shows the spectrum of the S_2 state. Hence, there is a small on-

diagonal five-pulse contribution at (1.7, 1.7) MHz that is visible in part B, which is not observed in part A.

7. 2D ^{13}C HYSCORE spectroscopy of the S_2 state of ^{13}C-methanol-treated WT PSII from *Synechocystis* sp. PCC 6803.
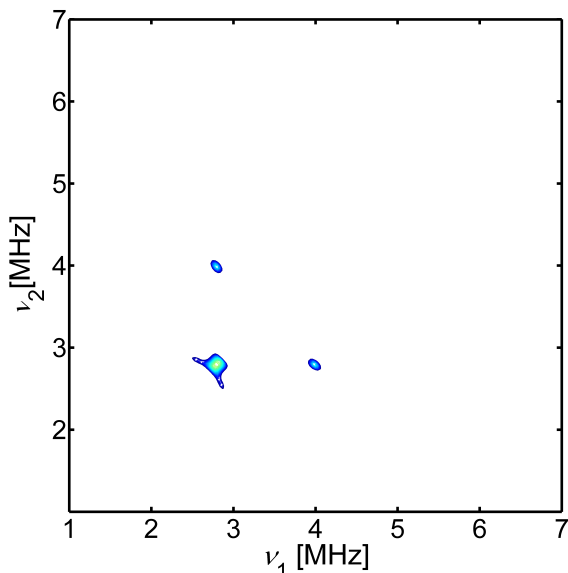

Figure 4S. Experimental contour-plot representation of the (+, +) quadrant of the 2D ^{13}C HYSCORE spectrum of the S_2 state of the OEC of ^{13}C-methanol-treated PSII from *Synechocystis* sp. PCC 6803. The spectrum was acquired at a magnetic field of 335.0 mT and temperature of 5 K. As can be seen, the intense cross-peaks at (5.4, 2.1) and (2.1, 5.4) MHz are not observed in this spectrum, indicating that ^{13}C-methanol is not bound to the OEC in the S_2 state of WT PSII.

8. QM/MM optimization of computational models of methanol binding in the S_2 state.
We constructed two-layer QM/MM models from PDB entry 3ARC[19] as described previously.[20] The sphere model included all residues with an alpha carbon atom within 15 Å of the OEC and all waters within the same distance. Cut protein chains were capped with an acetyl (ACE) or methylamine (NME) group at the N- and C-termini, respectively. The QM layer was comprised of the OEC and the side chains of all its ligands, as well as several second shell residues (D1-D61, D1-H337, and CP43-R357) and 10 water molecules (W_1-W_5, W_7-W_9, W_X, and W_Y). In the MM layer, capping residues, waters, and ions were frozen to encourage the model to hold its shape after its removal from the surrounding PSII environment. To optimize the hydrogen bond network, the hydrogen atoms of all waters were free to move. To bind methanol or methoxide to the OEC, either W_1 or W_2 was replaced with the desired molecule and the QM/MM

model was optimized. All calculations were performed using the Gaussian 16[21] software package with the B3LYP[22] functional for the QM layer and the Amber[23] force field for the MM layer. Within the QM layer, the 6-31G(d)[24-26] basis was applied to carbon, nitrogen, oxygen, and hydrogen atoms and the LaNL2DZ[27] basis set and pseudopotential was applied to manganese and calcium atoms.

9. Density Functional Theory calculations. We used the coordinates from QM/MM models of the S_2 state to perform DFT calculations using the software package, ORCA 4.1.2.[28] The QM layer of the three computational models Mn4-W1, Mn4-W2 and Mn1-MeOH containing the Mn_4Ca-oxo cluster, amino acid residues, bound methoxy/methanol and water ligands (**Figure 3A-C**) were used for density functional theory (DFT) calculations in the high-spin (high-spin, $M_S = S' = {}^{13}/_2$) state and then in the broken-symmetry (BS) (low-spin, $M_S = {}^1/_2$) state by flipping of electronic spins at two of the four Mn centers using the "FlipSpin" routine of ORCA to produce a low-spin $S' = ½$ ground state (doublet). The calculations used both hybrid- and hybrid meta-generalized gradient approximation (GGA) B3LYP and TPSSh functionals with the split-valence polarization (SVP) basis set,[29, 30] utilizing the effective core potential (ECP or pseudopotential) approximation to include valence electrons and to replace core electrons. By using the resolution of identity approximation (RI), these calculations were complemented with the decontracted auxiliary basis set, *i.e.* Coulomb fitting def2/J[31-34] implemented in Orca 4.0.1,[35] that decreased the computational time significantly and the TZVP basis set[29, 30] along with the chain of spheres (RIJCOSX)[36] approximation to exact exchange using the same decontracted auxiliary basis set was replaced for heavier manganese (Mn) atoms. The calculations used a conductor-like polarizable continuum model (CPCM) with a dielectric constant of $\varepsilon = 80.4$[37] and included an atom-pairwise dispersion correction with the Becke-Johnson damping scheme (D3BJ),[38, 39] a third generation (D3) semi-empirical van der Waals correction. All the optimized geometries converged successfully. The calculations for the ${}^{13}C$ hyperfine interactions were carried out in spin-unrestricted mode. BS-DFT calculations were performed on each model in terms of single and double spin flips to compute the six pairwise exchange coupling constants Jij that parameterize the magnetic coupling between the four Mn ions in an Ising-type Hamiltonian in order to determine the model that is compatible with experimental hyperfine parameters that were obtained from the 2D ${}^{13}C$ HYSCORE measurements. Specific details of hyperfine coupling calculations were consistent with previous theoretical methodologies[40] and the

calculated ^{13}C isotropic hyperfine (A_{iso}) couplings were rescaled using the empirical factors derived for the B3LYP and TPSSh as described previously.[41, 42]

9.1. *Evaluation of exchange interaction parameters*.

The electronic structure of Mn_4Ca-oxo cluster in the OEC is defined by a set of six pairwise Mn – Mn exchange interaction terms J_{ij}, that were calculated using BS-DFT. Diagonalization of the Heisenberg Hamiltonian to obtain the complete spin-ladder was used to confirm the effective $S = \frac{1}{2}$ ground state (low-spin) in antiferromagnetic interaction. Details on the prediction of exchange interactions and magnetic properties are described in references.[43-45]

Table 2S. BS-DFT calculated exchange interaction constants J (in cm^{-1}) of the two Mn4 models. The BS-DFT calculation employed B3LYP[a] and TPSSh[b] functional, respectively. The units for the exchange coupling constants, J, are in cm^{-1}.

Model	Mn4-W2	Mn4-W1
	-10.36	-6.14
J^a	-8.98	-5.33
	-10.40	-6.17
	-12.98	-4.98
J^b	-11.25	-4.32
	-13.02	-4.99

As shown in Table 2S, the exchange coupling constants, J, were calculated from the Noodleman (1st row), Benchini (2nd row), and Yamaguchi (3rd row) coupling schemes.[46, 47 48 49, 50 51] In general, the third scheme covered all possible mechanisms of spin exchange interactions from the strong to the weak coupling limit.[46, 48] We observed that the magnitude of exchange interaction values were not sensitive to the choice of functional and basis set used in BS-DFT calculations for the computational models. It was also evident from the BS-DFT calculations that the clusters were weakly antiferromagnetically coupled systems with negative exchange coupling constants, J.

The exchange interactions in the OEC are not described in detail as it is not the primary focus of the DFT calculations. Moreover, it is meaningless to interpret the calculated J couplings or perform comparisons with experimental data since the observed ground state and measured energy differences between magnetic levels in the spin-ladder representation could significantly deviate for real and model systems, depending on the number of potential spin eigen states available in molecular topologies

of the atomic compositions. It is also important to note that BS-DFT solutions are not spin eigen functions. Nevertheless, the calculated values using the TPSSh functional are in agreement with the range of exchange couplings obtained for previous OEC models employing similar DFT functionals and basis sets.[52]

9.2. *Calculation of the spin Hamiltonian parameters*.

The DFT calculations employed hybrid-GGA B3LYP[22, 53, 54] and hybrid meta-GGA TPSSh[55] functionals to calculate the spin-Hamiltonian parameters. The split-valence polarization (SVP) [29, 30] basis set was used for lighter atoms, such as C, N, O and H and the triple-zeta valence polarization (TZVP)[29, 30] basis set was utilized with the auxiliary basis set[31-34] for heavier manganese (Mn) atoms. For comparison, we also performed single point calculations of isotropic hyperfine coupling constants using B3LYP and TPSSh approximations with the EPR optimized EPR-II basis set.[56] These afforded comparisons of calculated spin densities and ^{13}C hyperfine coupling constants with calculations using hybrid and meta-hybrid functionals with Ahlrich basis set.

We calculated the ^{13}C hyperfine coupling constants with the TPSSh functional combined with triple-zeta ZORA-recontracted basis set on carbon atom, including the relativistic picture-change effect. In this case, calculations used the zeroth-order regular approximation (ZORA)[57, 58, 59] Hamiltonian to include scalar relativistic effects. ZORA adapted segmented all-electron relativistically contracted (SARC/J)[60] auxiliary basis sets were employed for optimizations, and the TZVP [29, 30] basis set was replaced for manganese atoms as well. In principle, nuclear hyperfine and quadrupole coupling constants can be calculated for ^{55}Mn, ^{14}N and ^{17}O using the chain of spheres (RIJCOSX)[36] approximation for comparisons. However, the main focus of this study was to calculate the ^{13}C hyperfine couplings and to the calculated values with the experimental ^{13}C HYSCORE results. The BP86 functional[53, 61] is known to be not reliable for heavier atoms, so was not used in our DFT calculations of ^{13}C hyperfine coupling constants.

9.2.1. *Calculated g-tensors*.

The Mn_4Ca-oxo cluster in the S_2 state of the OEC cluster is in an $S' = \frac{1}{2}$ ground state, as established by antiferromagnetic exchange couplings between the electron spins of adjacent Mn ions. Shown in **Table 3S** are the calculated **g**-tensor components (non spin-projected) of the QM layer of the Mn4-W2, Mn4-W1 and Mn1-MeOH computational models. The **g**-tensors confirmed the low-spin ground ($S' = \frac{1}{2}$) state of the S_2 state. For all three models, the calculated isotropic values of the **g**-tensor are very close to the free

electron g_e value. In addition, the g_3 (or g_z) component of the **g**-tensor is slightly larger than the free electron g_e value, indicating that there is an admixture from *d*-orbitals of managnese ions to electron spin density. This component of the **g**-tensor typically coincides with the S_2-state principal axis of the low-spin manganese cluster with respect to the direction of the applied magnetic field.

Table 3S. Calculated **g**-tensor components using the TPSSh functional with the EPR-II or ZORA/TZVP basis set.

Model	EPR-II				ZORA/TZVP			
	g_x	g_y	g_z	g_{iso}	g_x	g_y	g_z	g_{iso}
Mn₄-W₂	1.9912	2.0147	2.0164	2.0074	1.9917	2.0145	2.0168	2.0076
Mn₄-W₁	1.9765	2.0035	2.0222	2.0007	1.9773	2.0031	2.0220	2.0008
Mn₁-MeOH	1.9967	2.0092	2.0194	2.0083	1.9988	2.0038	2.0071	2.0032

9.2.2. ^{13}C *hyperfine interactions*.

The Mn4-W1 and Mn4-W2 models contain a deprotonated methoxide group that binds to the dangler manganese Mn4 site in the first coordination sphere, whereas Mn1-MeOH contains a methanol molecule binding at the Mn1 site of the Mn_4Ca-oxo cluster in the S_2 state. The hybrid functional calculations used in this work present an opportunity to calculate the ^{13}C hyperfine coupling constants of bound methoxide or methanol for direct comparison with the experimental couplings determined by the ^{13}C HYSCORE analysis. It was previously demonstrated that the B3LYP functional tends to significantly underestimate ^{55}Mn isotropic hyperfine coupling constant.[42, 62] An approximate spin-projection approach has to be used to rescale the isotropic and anisotropic hyperfine constants calculated for ^{13}C. A scaling factor of 1.59 and 1.53 was determined to be suitable for the B3LYP and TPSSh functional, respectively.[41] Thus, we rescaled the calculated ^{13}C couplings by a factor of 1.59 in **Table 4S** and **5S**. The calculated ^{13}C A_{iso} and T values for model Mn4-W2 are in close agreement with experimental coupling constants that were measured by ^{13}C HYSCORE.

Table 4S. Rescaled calculated ^{13}C-hyperfine couplings using the B3LYP functional with the EPR-II or ZORA/TZVP basis set.

	EPR-II		ZORA/TZVP	
Model	A_{iso}	T	A_{iso}	T
Mn$_4$-W$_2$	3.38	1.78	3.36	1.78
Mn$_4$-W$_1$	8.30	7.89	1.0	2.69
Mn$_1$-MeOH	1.68	1.75	1.60	1.80

Table 5S. Rescaled ^{13}C-hyperfine couplings using the TPSSh functional with the EPR-II or ZORA/TZVP basis set.

	EPR-II		ZORA/TZVP	
Model	A_{iso}	T	A_{iso}	T
Mn$_4$-W$_2$	3.23	1.89	3.37	1.90
Mn$_4$-W$_1$	0.86	2.09	0.33	2.98
Mn$_1$-MeOH	1.53	1.78	1.89	1.75

References.

[1] Debus, R. J., Campbell, K. A., Gregor, W., Li, Z. L., Burnap, R. L., and Britt, R. D. (2001) Does Histidine 332 of the D1 Polypeptide Ligate the Manganese Cluster in Photosystem II? An Electron Spin Echo Envelope Modulation Study, *Biochemistry 40*, 3690-3699.

[2] Debus, R. J. (2014) Evidence from FTIR Difference Spectroscopy That D1-Asp61 Influences the Water Reactions of the Oxygen-Evolving Mn$_4$CaO$_5$ Cluster of Photosystem II, *Biochemistry 53*, 2941-2955.

[3] Strickler, M. A., Walker, L. M., Hillier, W., and Debus, R. J. (2005) Evidence from Biosynthetically Incorporated Strontium and FTIR Difference Spectroscopy that the C-terminus of the D1 Polypeptide of Photosystem II Does Not Ligate Calcium, *Biochemistry 44*, 8571–8577.

[4] Oyala, P. H., Stich, T. A., Stull, J. A., Yu, F., Pecoraro, V. L., and Britt, R. D. (2014) Pulse Electron Paramagnetic Resonance Studies of the Interaction of Methanol with the S$_2$ State of the Mn$_4$O$_5$Ca Cluster of Photosystem II, *Biochemistry 53*, 7914–7928.

[5] Höfer, P., Grupp, A., Nebenführ, H., and Mehring, M. M. (1986) Hyperfine Sublevel Correlation (HYSCORE) Spectroscopy: A 2D ESR Investigation of the Squaric Acid Radical, *Chem. Phys. Lett. 132*, 279–282.

[6] Chatterjee, R., Milikisiyants, S., Coates, C. S., and Lakshmi, K. V. (2011) High-Resolution Two-Dimensional ^{1}H and ^{14}N Hyperfine Sublevel Correlation Spectroscopy of the Primary Quinone of Photosystem II, *Biochemistry 50*, 491-501.

[7] Milikisiyants, S., Chatterjee, R., Weyers, A., Meenaghan, A., Coates, C., and Lakshmi, K. V. (2010) Ligand Environment of the S_2 State of Photosystem II: A Study of the Hyperfine Interactions of the Tetranuclear Manganese Cluster by 2D ^{14}N HYSCORE Spectroscopy, *J. Phys. Chem. B 114*, 10905-10911.

[8] Dikanov, S. A., and Tsvetkov, Y. D. (1992) *Electron Spin Echo Envelope Modulation (ESEEM) Spectroscopy*, CRC Press, Boca Raton, FL.

[9] Schweiger, A., and Jeschke, G. (2001) *Principles of Pulse Electron Paramagnetic Resonance*, Oxford University Press.

[10] Gemperle, C., Aebli, G., Schweiger, A., and Ernst, R. R. (1990) Phase Cycling in Pulse EPR, *J. Magn. Reson. 88*, 241-256.

[11] Gemperle, C., Schweiger, A., and Ernst, R. R. (1991) Electron-spin-echo Envelope Modulation With Improved Modulation Depth, *Chem. Phys. Lett. 178*, 565-572.

[12] Song, R., Zhong, Y. C., Noble, C. J., Pilbrow, R., and Hutton, D. R. (1995) A New Six-pulse Two-dimensional Electron Spin Echo Envelope Modulation (ESEEM) Correlation Spectroscopy, *Chem. Phys. Lett. 237*, 86-90.

[13] Kasumaj, B., and Stoll, S. (2008) 5- and 6-Pulse Electron Spin Echo Envelope Modulation (ESEEM) of Multi-nuclear Spin Systems, *J. Magn. Reson. 190*, 233-247.

[14] Dikanov, S. A., and Bowman, M. K. (1995) Cross-Peak Lineshape of Two-Dimensional ESEEM Spectra in Disordered S = 1/2, I = 1/2 Spin Systems, *J. Magn. Reson., Ser. A 116*, 125-128.

[15] Dikanov, S. A., Tyryshkin, A. M., and Bowman, M. K. (2000) Intensity of Cross-Peaks in Hyscore Spectra of S = 1/2, I = 1/2 Spin Systems, *J. Magn. Reson. 144*, 228-242.

[16] Stoll, S., and Schweiger, A. (2006) EasySpin, A Comprehensive Software Package for Spectral Simulation and Analysis in EPR, *J. Magn. Reson. 178*, 42-55.

[17] Stoll, S., and Britt, R. D. (2009) General and Efficient Simulation of Pulse EPR Spectra, *Phys. Chem. Chem. Phys. 11*, 6614-6625.

[18] Dikanov, S. A., and Taguchi, A. T. (2018) Two-Dimensional Pulsed EPR Resolves Hyperfine Coupling Strain in Nitrogen Hydrogen Bond Donors of Semiquinone Intermediates, *J. Phys. Chem. B 122*, 5205-5211.

[19] Umena, Y., Kawakami, K., Shen, J. R., and Kamiya, N. (2011) Crystal Structure of Oxygen-evolving Photosystem II at a Resolution of 1.9 Angstrom, *Nature 473*, 55-65.

[20] Luber, S., Rivalta, I., Umena, Y., Kawakami, K., Shen, J.-R., Kamiya, N., Brudvig, G. W., and Batista, V. S. (2011) S_1-state Model of the O_2-evolving Complex of Photosystem II, *Biochemistry 50*, 6308-6311.

[21] Frisch, M. J., Trucks, G. W., Schlegel, H. B., Scuseria, G. E., Robb, M. A., Cheeseman, J. R., Scalmani, G., Barone, V., Petersson, G. A., Nakatsuji, H., Li, X., Caricato, M., Marenich, A. V., Bloino, J., Janesko, B. G., Gomperts, R., Mennucci, B., Hratchian, H. P., Ortiz, J. V., Izmaylov, A. F., Sonnenberg, J. L., Williams, Ding, F., Lipparini, F., Egidi, F., Goings, J., Peng, B., Petrone, A., Henderson, T., Ranasinghe, D., Zakrzewski, V. G., Gao, J., Rega, N., Zheng, G., Liang, W., Hada, M., Ehara, M., Toyota, K., Fukuda, R., Hasegawa, J., Ishida, M., Nakajima, T., Honda, Y., Kitao, O., Nakai, H., Vreven, T., Throssell, K., Montgomery Jr., J. A., Peralta, J. E., Ogliaro, F., Bearpark, M. J., Heyd, J. J., Brothers, E. N., Kudin, K. N., Staroverov, V. N., Keith, T. A., Kobayashi, R., Normand, J., Raghavachari, K., Rendell, A. P., Burant, J. C., Iyengar, S. S., Tomasi, J., Cossi, M., Millam, J. M., Klene, M., Adamo, C., Cammi, R., Ochterski, J. W., Martin, R. L., Morokuma, K., Farkas, O., Foresman, J. B., and Fox, D. J. (2016) *Gaussian 16 {R}evision {C}.01*, Vol. C.01, Wallingford, CT.

[22] Becke, A. D. (1993) Density-functional Thermochemistry. III. The Role of Exact Exchange, *J. Chem. Phys. 98*, 5648-5652.

[23] Cornell, W. D., Cieplak, P., Bayly, C. I., Gould, I. R., Jr., K. M. M., Ferguson, D. M., Spellmeyer, D. C., Fox, T., Caldwell, J. W., and Kollman, P. A. (1995) A Second Generation Force-field for the Simulation of Proteins, Nucleic-acids, and Organic Molecules, *J. Am. Chem. Soc. 117*, 5179-5197.

[24] Ditchfield, R., Hehre, W. J., and Pople, J. A. (1971) Self-Consistent Molecular Orbital Methods. 9. Extended Gaussian-type Basis for Molecular-orbital Studies of Organic Molecules, *J. Chem. Phys. 54*, 724.

[25] Hariharan, P. C., and Pople, J. A. (1973) Influence of Polarization Functions on Molecular-orbital Hydrogenation Energies, *Theor. Chem. Acc. 28*, 213-222.

[26] Hehre, W. J., Ditchfield, R., and Pople, J. A. (1972) Self-Consistent Molecular Orbital Methods. 12. Further Extensions of Gaussian-type Basis Sets for Use in Molecular-orbital Studies of Organic Molecules, *J. Chem. Phys. 56*, 2257.

[27] Hay, P. J., and Wadt , W. R. (1985) Ab Initio Effective Core Potentials for Molecular Calculations. Potentials for K to Au Including the Outermost Core Orbitals, *J. Chem. Phys. 82*, 299-310.

[28] Neese, F. (2018) Software update: the ORCA program system, version 4.0, *WIREs Comput. Mol. Sci. 8*, e1327.

[29] Weigend, F., and Ahlrichs, R. (2005) Balanced Basis Sets of Split Valence, Triple Zeta Valence and Quadruple Zeta Valence Quality for H to Rn: Design and Assessment of Accuracy, *Phys. Chem. Chem. Phys. 7*, 3297-3305.

[30] Schaefer, A., Horn, H., and Ahlrihcs, R. (1992) Fully Optimized Contracted Gaussian Basis Sets for Atoms Li to Kr, *J. Chem. Phys. 97*, 2571-2577.

[31] Weigend, F. (2006) Accurate Coulomb-fitting Basis Sets for H to Rn, *Phys. Chem. Chem. Phys. 8*, 1057-1065.

[32] Eichkorn, K., Weigend, F., Treutler, O., and Ahlrichs, R. (1997) Auxiliary Basis Sets for Main Row Atoms and Transition Metals and Their Use to Approximate Coulomb Potentials, *Theor. Chem. Acc. 97*, 119-124.

[33] Eichkorn, K., Treutler, O., Oehm, H., Haeser, M., and Ahlrichs, R. (1995) Auxiliary Basis Sets to Approximate Coulomb Potentials, *Chem. Phys. Lett. 240*, 283-290.

[34] Eichkorn, K., Treutler, O., Oehm, H., Haeser, M., and Ahlrichs, R. (1995) Erratum, Auxiliary Basis Sets to Approximate Coulomb Potentials, *Chem. Phys. Lett. 242*, 652-660.

[35] Neese, F. (2012) The ORCA Program System, *WIREs Comput. Molec. Sci. 2*, 73-78.

[36] Neese, F., Wennmohs, F., Hansen, A., and Becker, U. (2009) Efficient, Approximate and Parallel Hartree-Fock and Hybrid DFT Calculations. A 'Chain-of-spheres' Algorithm for the Hartree-Fock Exchange, *Chem. Phys. 356*, 98-109.

[37] Klamt, A., and Schuurmann, G. (1993) COSMO: A New Approach to Dielectric Screening in Solvents With Explicit Expressions for the Screening Energy and Its Gradient, *J. Chem. Soc., Perkin Trans. 2*, 799-805.

[38] Grimme, S., Ehrlich, S., and Goerigk, L. (2011) Effect of the Damping Function in Dispersion Corrected Density Functional Theory, *J. Comput. Chem. 32*, 1456–1465.

[39] Grimme, S., Antony, J., Ehrlich, S., and Krieg, H. (2010) A Consistent and Accurate Ab Initio Parametrization of Density Functional Dispersion Correction (DFT-D) for the 94 Elements H-Pu, *J. Chem. Phys. 132*, 154104.

[40] Lohmiller, T., Krewald, V., Navarro, M. P., Retegan, M., Rapatskiy, L., Nowaczyk, M. M., Boussac, A., Neese, F., Lubitz, W., Pantazis, D. A., and Cox, N. (2014) Structure, Ligands

and Substrate Coordination of the Oxygen-evolving Complex of Photosystem II in the S_2 State: A Combined EPR and DFT Study, *Phys. Chem. Chem. Phys. 16*, 11877–11892.

[41] Pantazis, D. A., Orio, M., Petrenko, T., Zein, S., Lubitz, W., Messinger, J., and Neese, F. (2009) Structure of the Oxygen-evolving Complex of Photosystem II: Information on the S_2 State Through Quantum Chemical Calculation of Its Magnetic Properties, *Phys. Chem. Chem. Phys. 11*, 6788–6798.

[42] Pantazis, D. A., Orio, M., Petrenko, T., Zein, S., Bill, E., Lubitz, W., Messinger, J., and Neese, F. (2009) A New Quantum Chemical Approach to the Magnetic Properties of Oligonuclear Transition-Metal Complexes: Application to a Model for the Tetranuclear Manganese Cluster of Photosystem II, *Chem. Eur. J. 15*, 5108-5123.

[43] Krewald, V., Neese, F., and Pantazis, D. A. (2013) On the Magnetic and Spectroscopic Properties of High-Valent Mn_3CaO_4 Cubanes as Structural Units of Natural and Artificial Water-oxidizing Catalysts, *J. Am. Chem. Soc. 135*, 5726-5739.

[44] Orio, M., Pantazis, D. A., Petrenko, T., and Neese, F. (2009) Magnetic and Spectroscopic Properties of Mixed Valence Manganese(III,IV) Dimers: A Systematic Study Using Broken Symmetry Density Functional Theory, *Inorg. Chem. 48*, 7251-7260.

[45] Sinnecker, S., Neese, F., Noodleman, L., and Lubitz, W. (2004) Calculating the Electron Paramagnetic Resonance Parameters of Exchange Coupled Transition Metal Complexes Using Broken Symmetry Density Functional Theory: Application to a MnIII/MnIV Model Compound, *J. Am. Chem. Soc. 126*, 2613-2622.

[46] Soda, T., Kitagawa, Y., Takano, Y., Shigeta, Y., Nagao, H., Yoshioka, Y., and Yamaguchi, K. (2000) Ab Initio computations of Effective Exchange Integrals for H–H, H–He–H and Mn_2O_2 Complex: Comparison of Broken-symmetry Approaches, *Chem. Phys. Lett. 319*, 223-230.

[47] Noodleman, L., and Davidson, E. R. (1986) Ligand Spin Polarization and Antiferromagnetic Coupling in Transition Metal Dimers, *Chem. Phys. 109*, 131-141.

[48] Yamaguchi, K., Takahara, Y., and Fueno, T. (1986) Applied Quantum Chemistry, (Smith, V. H., Ed.), p 155, Reidel, Dordrecht, The Netherlands.

[49] Noodleman, L. (1981) Valence Bond Description of Antiferromagnetic Coupling in Transition Metal Dimers *J. Chem. Phys. 74*, 5737-5743.

[50] Ginsberg, A. P. (1980) Magnetic Exchange in Transition Metal Complexes. 12. Calculation of Cluster Exchange Coupling Constants with the X.alpha.-Scattered Wave Method, *J. Am. Chem. Soc. 102*, 111-117.

[51] Bencini, A., and Gatteschi, D. (1980) X.alpha.-SW Calculations of the Electronic Structure and Magnetic Properties of Weakly Coupled Transition-metal Clusters. The $[Cu_2Cl_6]_2$-Dimers, *J. Am. Chem. Soc. 108*, 5763-5771.

[52] Retegan, M., and Pantazis, D. A. (2016) Interaction of Methanol with the Oxygen-evolving Complex: Atomistic Models, Channel Identification, Species Dependence, and Mechanistic Implications, *Chem. Sci. 216*, 6463–6476.

[53] Becke, A. D. (1988) Density-functional Exchange-energy Approximation With Correct Asymptotic Behavior, *Phys. Rev. A 38*, 3098-3100.

[54] Lee, C., Yang, W., and Parr, R. G. (1988) Development of the Colle-Salvetti Correlation-energy Formula Into a Functional of the Electron Density, *Phys. Rev. B 37*, 785-789.

[55] Staroverov, V. N., Scuseria, G. E., Tao, J., and Perdew, J. P. (2003) Comparative Assessment of a New Nonempirical Density Functional: Molecules and Hydrogen-bonded Complexes, *J. Chem. Phys. 119*, 12129-12137.

[56] Barone, V. (1995) In *Recent Advances in Density Functional Methods Part 1* (Chong, D. P., Ed.), p 287, World Scientific, Singapore.

[57] van Wüllen, C. (1998) Molecular Density Functional Calculations in the Regular Relativistic Approximation: Method, Application to Coinage Metal Diatomics, Hydrides, Fluorides and Chlorides, and Comparison With First-order Relativistic Calculations, *J. Chem. Phys. 109*, 392-399.

[58] van Lenthe, E., Baerends, E. J., and Snijders, J. G. (1994) Relativistic Total Energy Using Regular Approximations, *J. Chem. Phys. 101*, 9783-9792.

[59] van Lenthe, E., Baerends, E. J., and Snijders, J. G. (1993) Relativistic Regular Two‐component Hamiltonians, *J. Chem. Phys. 99*, 4597-4610.

[60] Pantazis, D. A., and Neese, F. (2012) All-electron Scalar Relativistic Basis Sets for the 6p Elements, *Theor. Chem. Acc. 131*, 1292-1298.

[61] Perdew, J. (1986) Density-functional Approximation for the Correlation Energy of the Inhomogeneous Electron Gas, *Phys. Rev. B 33*, 8822-8824.

[62] Munzarova, M., and Kaupp, M. (1999) A Critical Validation of Density Functional and Coupled-Cluster Approaches for the Calculation of EPR Hyperfine Coupling Constants in Transition Metal Complexes, *J. Phys. Chem. A 103*, 9966-9983.